ACS Catalysis

pubs.acs.org/acscatalysis

Research Article

Subnano-FeO_x Clusters Anchored in an Ultrathin Amorphous Al_2O_3 Nanosheet for Styrene Epoxidation

Zhao Yang,[§] Shuo Zhang,[§] Hewei Zhao, Anran Li, Long Luo,* and Lin Guo*

Cite This: *ACS Catal.* 2021, 11, 11542−11550

Read Online

ACCESS | Metrics & More | Article Recommendations | Supporting Information

ABSTRACT: The development of low-cost, high-performance catalysts at the atomic level has drawn scientists' attention due to the high atom efficiency, unique structure, and potentially high catalytic selectivity. Among the atomically tailored catalysts, nanoclusters are of particular interest because they represent an underexplored medium state between isolated single atoms and typical nanoparticles. In this study, we report a wet-chemistry approach to synthesize highly dispersed subnano-FeO_x clusters anchored on an ultrathin amorphous Al_2O_3 nanosheet (or Al_2O_3−FeO_x nanosheet) and its excellent catalytic performance for selective conversion of styrene to styrene oxide. The reasons for the high catalytic performance of the Al_2O_3−FeO_x nanosheet are 2-fold. One is that the unsaturated and amorphous nature of the Fe atoms in the subnano-FeO_x clusters promotes the adsorption of styrene onto the catalytic sites of FeO_x clusters for epoxidation. The other is that the amorphous Al_2O_3 nanosheet prevents the aggregation of catalytic FeO_x clusters during the epoxidation reaction because its defective structure immobilizes the FeO_x clusters.

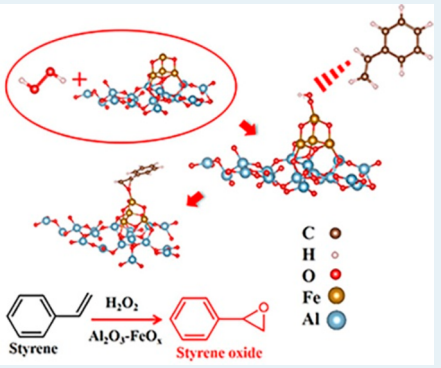

KEYWORDS: *2D material, subnanocluster, catalysis, styrene epoxidation, amorphous material*

INTRODUCTION

Nanoclusters are a new class of nanomaterials that typically contain from two to a few hundred atoms. Nanoclusters often show unique catalytic performance relative to their bulk counterparts due to the quantum confinement effect,[1−3] and more impressively, their properties are highly tunable at the atomic level.[4,5] Previous studies have demonstrated that noble metal nanoclusters exhibit significantly enhanced catalytic activities for the oxygen reduction reaction,[6,7] hydrogen evolution reaction,[8] and selective hydrogenation of nitrobenzene,[9] acetophenone,[10] and phenylacetylene.[11] The excellent catalytic activity of the noble metal nanoclusters was attributed to the large number of active sites of the nanoclusters and the strong interactions between the metallic nanoclusters and the support matrix. However, the real-world applications of these noble metal nanocluster catalysts are limited due to their high cost, scarcity, and poor long-term stability.[12,13] There is an unmet need for low-cost alternatives.

The 3d transition metals such as Fe, Co, and Ni are being studied to substitute for these noble metal-based catalysts.[14−16] Among these 3d transition metals, Fe is the most promising one due to its high natural abundance and tunable 3d orbital configuration. However, it remains challenging to anchor Fe species with high loading on a solid support while preventing the aggregation of Fe atoms or clusters into large particles during catalytic reactions, which causes the catalyst degradation. A popular strategy to overcome this challenge is to form coordination bonds between metal species with the functional groups of the solid support.[17,18] Previous studies have reported the use of ordered mesoporous carbon CMK-3,[19−21] pyrolyzed glucosamine,[22] and mesoporous graphitic carbon nitride[23] to support atomic Fe or Fe clusters.

Inspired by these prior studies, we developed a new Al_2O_3−FeO_x nanosheet material which uses ultrathin amorphous Al_2O_3 nanosheets rich in defects and dangling bonds as the support to dispense FeO_x nanoclusters with sizes < 1 nm. We tested the catalytic activity of the Al_2O_3−FeO_x nanosheet for styrene epoxidation to styrene oxide. The existing catalysts for styrene epoxidation reaction, such as Schiff base complexes,[24] multicomponent metal−organic framework derivatives,[25] and mixed metal oxides,[26] often have a low product selectivity and produce a mixture of styrene oxide and benzaldehyde. Here, we show that the Al_2O_3−FeO_x nanosheet catalyst addresses the selectivity challenge and achieves a high selectivity of 81% toward styrene oxide in 6 h. Even though the catalytic activity slowly decreased during consecutive runs due to the formation of organic pollutants on the Al_2O_3−FeO_x nanosheet catalyst, the catalyst can be fully regenerated by calcination, not achievable using commercial Al_2O_3−FeO_x catalyst.

Received: March 25, 2021
Revised: August 27, 2021
Published: September 2, 2021

https://doi.org/10.1021/acscatal.1c01366
ACS Catal. 2021, 11, 11542−11550

RESULTS AND DISCUSSION

We prepared the Al_2O_3−FeO_x nanosheets by mixing the $FeCl_3$ precursor with ultrathin amorphous Al_2O_3 nanosheets in deionized water. The Al_2O_3 nanosheets were first synthesized using a previously reported wet-chemical method.[27−30] The mixture of $FeCl_3$ and Al_2O_3 nanosheets was then freeze dried before being heated to 500 °C under a 5% H_2/Ar atmosphere for 2 h to produce the final Al_2O_3−FeO_x nanosheets. The Fe loading in Al_2O_3−FeO_x nanosheets can be adjusted by controlling the amount of $FeCl_3$ precursor. We use *n* %-Al_2O_3−FeO_x to name the Al_2O_3−FeO_x nanosheet samples, where *n*% is the weight ratio of $FeCl_3$ and Al_2O_3 in the synthesis. Figure 1a−e shows the high-angle annular dark field-

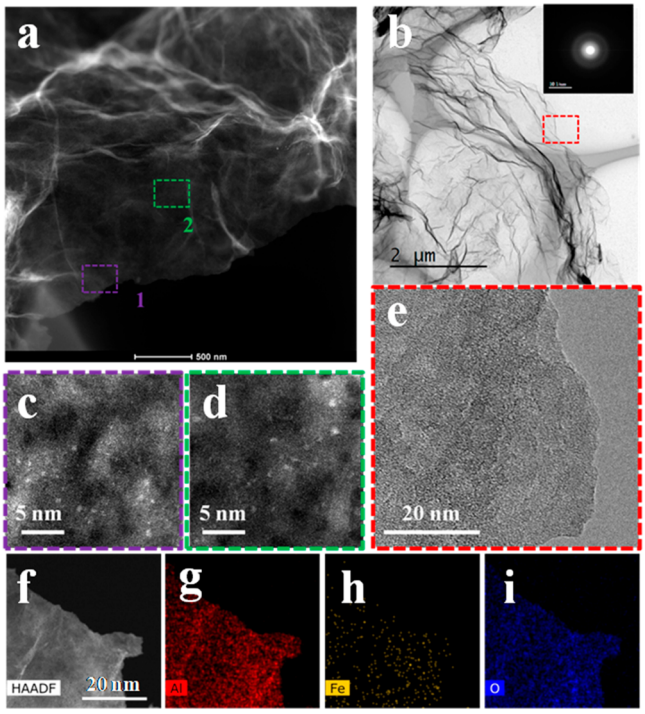

Figure 1. Structural characterization of Al_2O_3−FeO_x nanosheets. (a) HAADF-STEM image of Al_2O_3−FeO_x nanosheet catalyst with 6 wt % Fe loading, denoted as 6%-Al_2O_3−FeO_x. (b) TEM image with SAED inserted. (c and d) Expanded view of the HAADF images of the purple and green regions labeled in a. (e) HRTEM image captured at the red area in b. (f−i) HAADF-EDS mapping of Al, Fe, and O.

scanning transmission electron microscopy (HAADF-STEM) images (Figure 1a, 1c, and 1d) and the typical transmission electron microscopy (TEM) images (Figure 1b and 1e) of the 6%-Al_2O_3−FeO_x nanosheets: wrinkled nanosheet uniformly decorated with the subnano-FeO_x clusters (bright dots in Figure 1c and 1d). The selected area electron diffraction (SAED) pattern in Figure 1b (inset) shows a broad and diffused halo ring, indicating the amorphous state of the Al_2O_3 nanosheet. No particle aggregation was found in the TEM image (Figure 1e). The corresponding elemental mapping results in Figure 1f−i reveal that Al, O, and Fe were uniformly distributed across the nanosheet.

The Al_2O_3−FeO_x nanosheets with various Fe loadings were tested for catalytic epoxidation of styrene. The catalytic styrene epoxidation reaction could yield several products, including styrene oxide, benzaldehyde, benzoic acid, and 2-phenylacetaldehyde (Figure 2a). Styrene oxide is one of the most

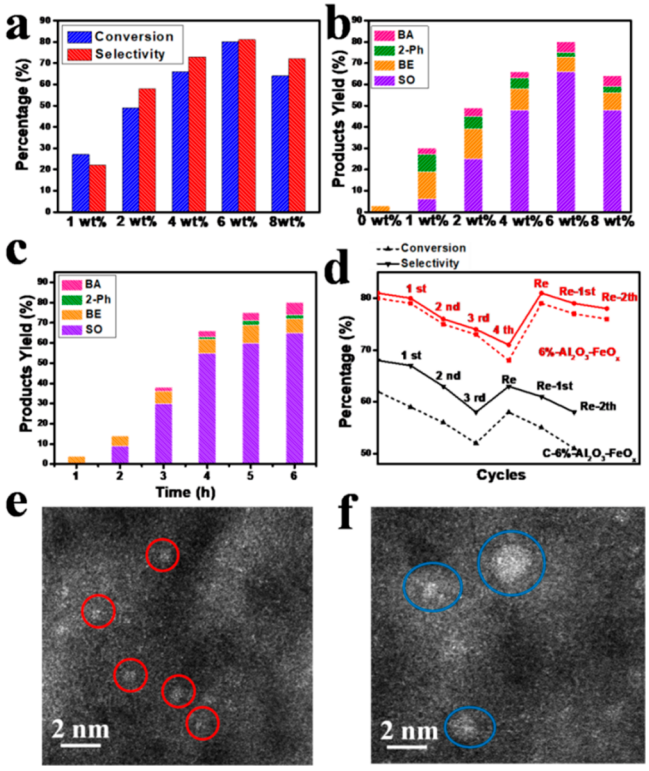

Figure 2. Catalytic performance of the Al_2O_3−FeO_x nanosheets for styrene epoxidation. (a) Molecular structures of styrene and its oxidized products. (b) Conversion and styrene oxide selectivity and (c) product yield distribution after 6 h reaction using Al_2O_3−FeO_x nanosheet catalysts with different Fe loadings. SO, styrene oxide; BE, benzaldehyde; 2-Ph, 2-phenylacetaldehyde; BA, benzoic acid. (d) Product yield distributions at different reaction times. (e) Comparison of the selectivity for styrene oxide (solid lines) and styrene conversion (dash lines) between 6%-Al_2O_3−FeO_x nanosheet catalyst (red) and C-6%-Al_2O_3−-FeO_x catalyst prepared using commercial Al_2O_3 nanoparticles as the support (black) during consecutive catalytic runs and after recalcination (Re). HAADF-STEM images of (f) 6%-Al_2O_3−FeO_x nanosheet catalyst and (g) C-6%-Al_2O_3−FeO_x control after recalcination. Bright dots marked with circles are FeO_x species.

valuable products due to its use in the synthesis of epoxy resin, UV (ultraviolet) absorbents, and pharmaceutical intermediates and the perfume industry. Figure 2b shows the 6%-Al_2O_3−FeO_x catalyst gives the highest styrene conversion of 80% and the highest selectivity of 81% for styrene oxide. A closer look at the product distribution in Figure 2c shows that the formation of 2-phenylacetaldehyde and benzaldehyde was suppressed with increasing Fe loading. The production of benzoic acid was always under 5%.

To understand the superior selectivity of the 6%-Al_2O_3−FeO_x catalyst, we performed the time-dependent product composition analysis to gain insights into the reaction pathways to different products. We sampled and analyzed the reaction mixture every hour (Figure 2d). In the first hour, benzaldehyde was observed, and no styrene oxide was produced. The conversion of styrene oxide began in the second hour and continued growing thereafter, whereas the conversion of benzaldehyde remained constant. The initial formation of benzaldehyde is possibly caused by the random and fast release of superoxide species ($O_2^{\bullet-}$) from H_2O_2,[31,32] where styrene would first transfer into styrene diol by direct

https://doi.org/10.1021/acscatal.1c01366
ACS Catal. 2021, 11, 11542−11550

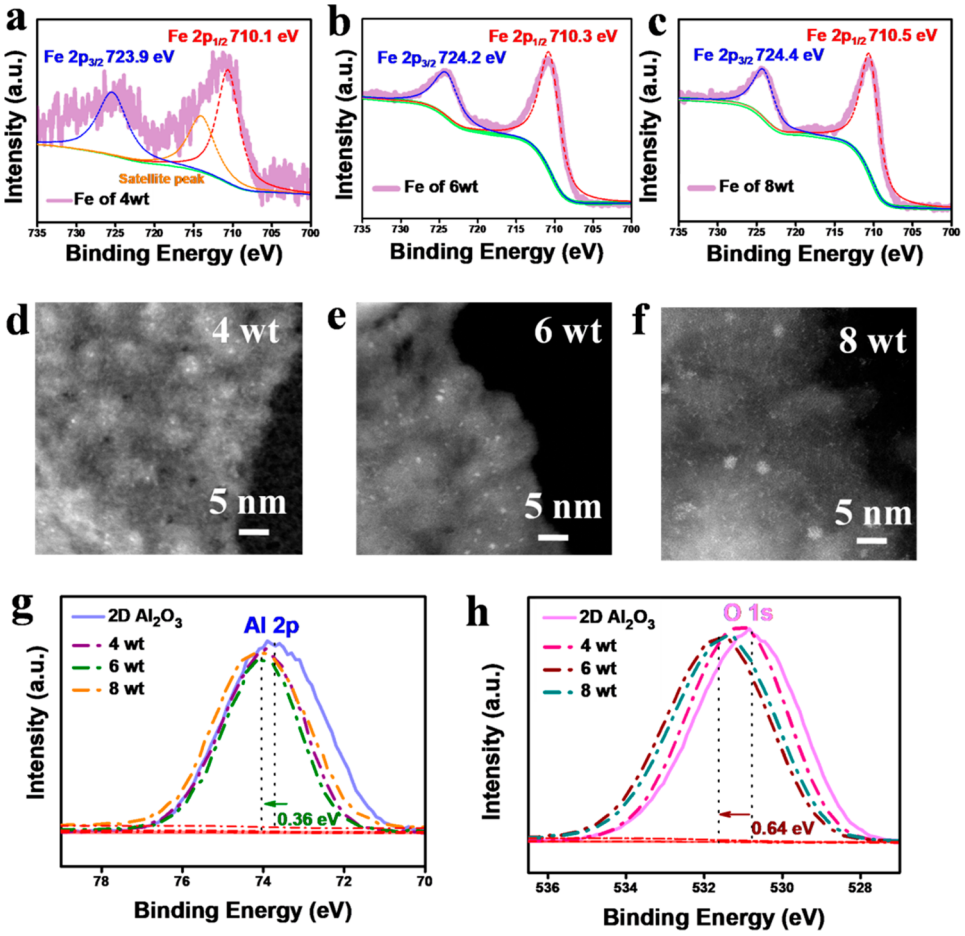

Figure 3. Electronic interactions between the FeO_x nanoclusters and the Al_2O_3 nanosheet. (a–c) XPS Fe 2p spectra and (d–f) corresponding HAADF-STEM images of Al_2O_3–FeO_x nanosheets with different Fe loadings. From left to right: 4%-, 6%-, and 8%-Al_2O_3–FeO_x. (g and h) XPS spectra of Al 2p and O 1s for pure Al_2O_3 nanosheet (2D Al_2O_3) and Al_2O_3–FeO_x nanosheets with different Fe loadings.

dihydroxylation, followed by oxidative cleavage via an unobserved α-hydroxy-carboxylic acid.[33] Unlike benzaldehyde, styrene oxide is produced by peroxidic species ($HOO^{\bullet-}$) from H_2O_2 attacking the C=C bond of styrene.[26] To verify the role of peroxidic species in styrene epoxidation, we introduced isopropyl alcohol, a radical scavenger. After the first hour of reaction, the selectivity for styrene oxide decreased to less than 5% (Figure S1). The possible reason for the suppressed formation of benzaldehyde after the first hour is that the Fe active sites of the Al_2O_3–FeO_x nanosheets could intercept the free peroxidic species ($HOO^{\bullet-}$) released from H_2O_2, forcing the styrene oxidation to proceed through the styrene oxide pathway. This explanation is partially supported by the observation that no styrene oxide was detected when using pure Al_2O_3 nanosheets without the Fe catalyst, while the yield of benzaldehyde was not affected. Besides styrene oxide and benzaldehyde, we also observed two minor products, benzoic acid and 2-phenylacetaldehyde. Benzoic acid is an oxidation product of benzaldehyde, and 2-phenylacetaldehyde is produced by the rearrangement of styrene oxide over Lewis acid sites.[34] The yield of 2-phenylacetaldehyde was also suppressed by the increasing Fe loading, suggesting that FeO_x clusters can suppress the ring-opening reaction.

After running styrene epoxidation tests consecutively 4 times, we observed a decrease in the catalytic activity for the 6%-Al_2O_3–FeO_x nanosheet catalyst in terms of styrene conversion and product selectivity (Figure 2e). Similar catalyst deactivation was observed in the control experiment using the C-6%-Al_2O_3–FeO_x catalyst prepared following the same synthetic method except with commercial Al_2O_3 power rather than the synthesized Al_2O_3 nanosheets. The catalyst deactivation is possibly caused by the accumulation of organic pollutants blocking the catalyst's active sites. The difference between the 6%-Al_2O_3–FeO_x nanosheet catalyst and the C-6%-Al_2O_3–FeO_x catalyst, however, is the ability to be regenerated by recalcination of the deactivated catalyst in air to remove the organic pollutants. After recalcination, styrene conversion using the 6%-Al_2O_3–FeO_x nanosheet catalyst was nearly fully recovered to 79%. In comparison, the recalcinated C-6%-Al_2O_3–FeO_x catalyst only shows a partial recovery of catalytic activity (Figure 2e). The difference in catalytic regeneration is caused by the higher thermal stability of the 6%-Al_2O_3–FeO_x nanosheet catalyst (the SEM (scanning electron microscopy) image is shown in Figure S2) than the C-6%-Al_2O_3–FeO_x catalyst (the SEM image is shown in Figure S3). The SEM images of the 6%-Al_2O_3–FeO_x nanosheet catalyst before and after recalcination show no noticeable change in the catalyst's morphology during recalcination (Figure S2). The X-ray diffraction patterns (Figure S4) of the 6%-Al_2O_3–FeO_x nanosheet catalyst before and after recalcination show that our nanosheet retains its amorphous feature, whereas the X-ray diffraction patterns of C–Al_2O_3–FeO_x can be indexed as α-Al_2O_3. Under HAADF-STEM, we did not observe any noticeable size change of the

https://doi.org/10.1021/acscatal.1c01366
ACS Catal. 2021, 11, 11542–11550

FeO_x nanoclusters for the 6%-Al_2O_3−FeO_x nanosheet catalyst (Figure 2f and Figure S5) either, indicating the high thermal stability of the 6%-Al_2O_3−FeO_x nanosheet catalyst. In contrast, the C-6%-Al_2O_3−FeO_x catalyst shows the aggregation of FeO_x clusters on the commercial Al_2O_3 support (Figure 2g and Figure S5), forming FeO_x particles with sizes over 2 nm. The size increase of the FeO_x clusters reduces the active sites, resulting in the permanent partial loss of catalytic activity after recalcination. The higher thermal stability of the 6%-Al_2O_3−FeO_x nanosheet catalyst than its commercial counterpart can be attributed to the large number of defect sites and cavities of Al_2O_3 nanosheets. These defective structures with dangling bonds were highly active for efficiently binding foreign elements, thus resulting in larger diffusion barriers to prevent the sintering of metal species via particle migration or Ostwald ripening.[35−38] Moreover, electron paramagnetic resonance (EPR) measurement was carried out to compare our Al_2O_3 amorphous nanosheet (2D Al_2O_3) and commercial Al_2O_3 nanoparticle (C−Al_2O_3), as shown in Figure S6. A clear signal in electron paramagnetic resonance results at g = 2.004 can be found with a 2D Al_2O_3 nanosheet, while the signal for C−Al_2O_3 was weaker, indicating a highly crystalline feature. The signal at g = 2.004 can be attributed to the presence of oxygen vacancies.[39,40] The difference in the EPR signal between the two Al_2O_3 supports suggested that our synthesized Al_2O_3 is rich in defects.

Thus far, we have shown the the FeO_x nanocluster sites of the Al_2O_3−FeO_x nanosheet catalyst are responsible for the high selectivity toward styrene oxide and that the Al_2O_3 nanosheet support is critical to the high thermal stability by immobilizing the active Fe species on its surface. Next, we investigated the role of the electronic interactions between the FeO_x nanoclusters and the Al_2O_3 nanosheet using X-ray photoelectron spectroscopy (XPS) to understand the catalytic activity trend for the Al_2O_3−FeO_x nanosheet catalysts with different Fe loadings. Figure 3a−c shows the XPS spectra of different Al_2O_3−FeO_x nanosheet catalysts in the Fe 2p region. Two characteristic peaks at around 710 eV for Fe 2p3/2 and 724 eV for Fe 2p1/2 indicate an approximately +3 valence state of Fe,[41,42] suggesting the Fe clusters can be referred to as "FeO_x". Moreover, we noticed a positive shift of the binding energy of Fe 2p with increasing Fe loading; thus, Fe 2p of 8%-Al_2O_3−FeO_x shows the highest binding energy among those Al_2O_3−FeO_x catalysts (1%-, 4%-, and 6%-Al_2O_3−FeO_x) (Figure 3a−c and Figure S7). The HAADF images in Figure 3d−f confirm that 4%-Al_2O_3−FeO_x has a smaller FeO_x cluster size than 6%- and 8%-Al_2O_3−FeO_x. Moreover, the HAADF image of 1%-Al_2O_3−FeO_x is shown in Figure S8; those HAADF images show the change from subnanoclusters of FeO_x to nanoparticles on increasing the Fe loading in the precursors. After running the styrene epoxidation test 4 times, there was no noticeable change in the Fe 2p region of the XPS spectra (Figure S9), suggesting the unchanged valence state of Fe after interacting with the oxidant. For the Al_2O_3 nanosheets, the binding energies of Al 2p and O 1s shift to lower values compared with that of bulk Al_2O_3[43] due to the lattice distortion of the amorphous Al_2O_3 nanosheet and extra chemical bond formation, shortening the interatomic distance and making electrons easier to hop over for both the Al and the O elements.[44,45] With Fe loadings, a constant positive shift of ∼0.36 eV for the Al 2p peaks was observed compared to the unloaded Al_2O_3 nanosheets (Figure 3g). In comparison, the shift of the O 1s peak in Figure 3h is more complex: 0.30, 0.64, and 0.58 eV for 4%-, 6%-, and 8%-Al_2O_3−FeO_x, respectively. The highest O 1s binding energy for 6%-Al_2O_3−FeO_x among the three Al_2O_3−FeO_x samples suggests more electrons transfer from Fe to O in 6%-Al_2O_3−FeO_x than in the other two Al_2O_3−FeO_x samples, which could favor the adsorption of styrene for catalytic epoxidation, leading to the highest catalytic activity of 6%-Al_2O_3−FeO_x. Besides the electron transfer effect, the FeO_x cluster size and density can also contribute to the highest catalytic activity of 6%-Al_2O_3−FeO_x as the STEM images in Figure 3d−f show that 6%-Al_2O_3−FeO_x has more FeO_x nanoclusters than 4%-Al_2O_3−FeO_x and a smaller nanocluster size than 8%-Al_2O_3−FeO_x.

We further measured the coordination environment of the Fe atoms in the Al_2O_3−FeO_x nanosheet catalysts using X-ray absorption spectroscopy. The X-ray absorption near-edge structure (XANES) spectra at the Fe K-edge are shown in Figure 4a. The valence state of Fe in 8%-Al_2O_3−FeO_x is close to that in α-Fe_2O_3, indicating a valence state of ∼+3, while the Fe K-edges of 1%-, 4%-, and 6%-Al_2O_3−FeO_x fall between FeO and α-Fe_2O_3, indicating a valence state between +2 and +3. This observation confirmed that nanoparticles (8%-Al_2O_3−FeO_x) have a higher oxidation state than subnanoclusters (1%-,

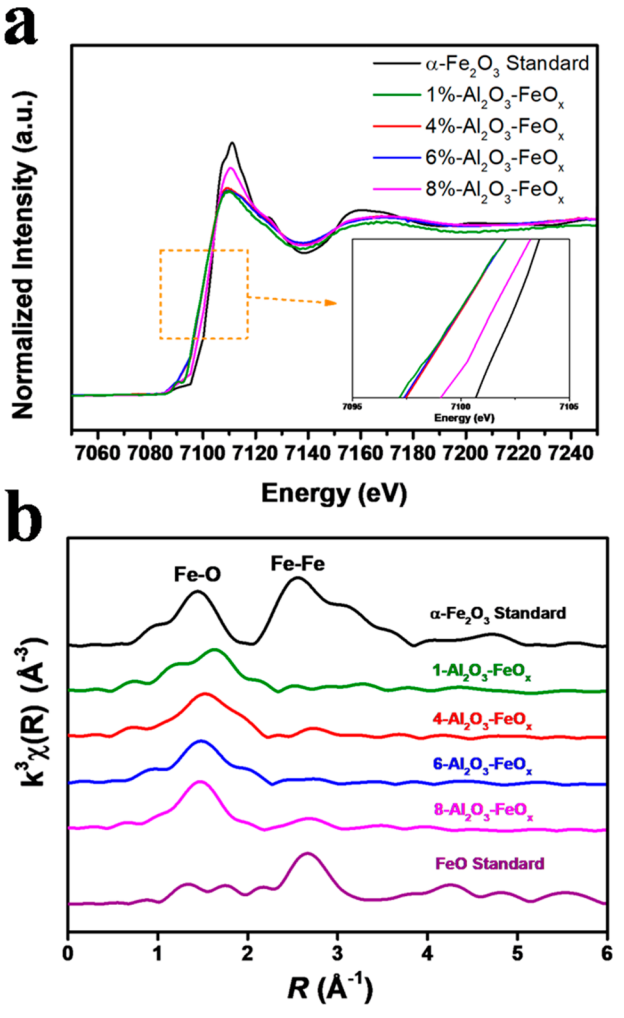

Figure 4. Measurements of the coordination environment of the Fe atoms in the Al_2O_3−FeO_x nanosheets using X-ray absorption spectroscopy. (a) Fe K-edge XANES spectra. (b) k^3-weighted Fourier transforms of Fe K-edge EXAFS spectra for FeO standard, α-Fe_2O_3 standard, and 1%-, 4%-, 6%-, and 8%-Al_2O_3−FeO_x.

https://doi.org/10.1021/acscatal.1c01366
ACS Catal. 2021, 11, 11542−11550

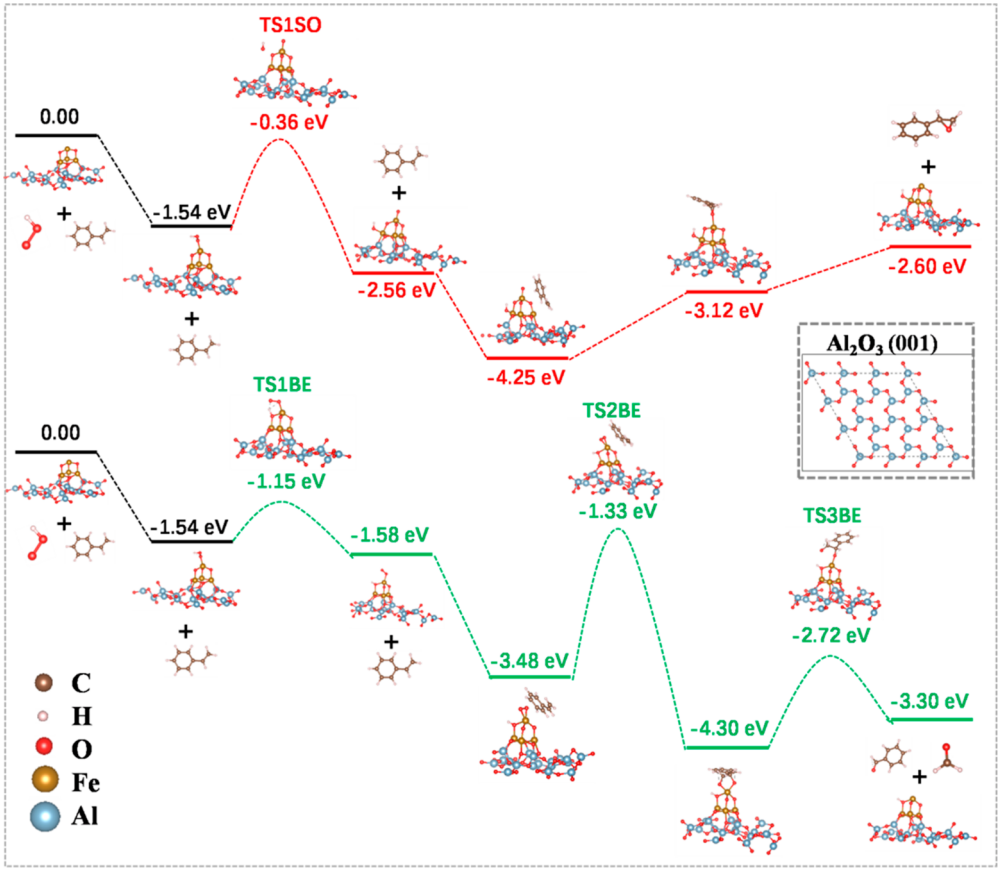

Figure 5. DFT-calculated energy diagrams for styrene oxidation to benzaldehyde and styrene oxide on a FeO_x cluster on the Al_2O_3 (001) facet.

4%-, and 6%-Al_2O_3−FeO_x). The XANES result was consistent with the XPS spectra. We performed Fourier-transformed extended X-ray absorption fine structure (FT-EXAFS) analysis (Figure 4b). The fitting result in Figure S10 and Table S1 shows that the Al_2O_3−FeO_x nanosheet catalysts show nearly 4-fold coordination, significantly lower than the 6-fold Fe−O coordination environment in α-Fe_2O_3. The significantly reduced coordination number is consistent with the sub-1 nm size of the FeO_x clusters in the HAADF-STEM images (Figures 1c, 1d, and 3d−f). The weak Fe−Fe scattering peak is also attributed to the ultrasmall size.[46] The X-ray absorption spectroscopy data reveals the unsaturated and amorphous nature of the Fe atoms in our catalyst, which should facilitate the adsorption of styrene for epoxidation. Meanwhile, H_2-temperature-programmed reduction (H_2-TPR) measurement was carried out to compare the reduction properties of subnanoclusters (1%, 6%-Al_2O_3−FeO_x) and nanoparticles (8%-Al_2O_3−FeO_x), as shown in Figure S11. The reduction peak of 8%-Al_2O_3−FeO_x at around 400 °C is related to the transition of Fe_2O_3 to Fe_3O_4, while the other peak at higher temperature can be attributed to the transition of Fe_3O_4 to FeO.[47] We also noticed that the reduction peak of 6%-Al_2O_3−FeO_x shifted to lower temperature compared with the other two catalysts. This indicated that 6%-Al_2O_3−FeO_x contributed the best catalytic performance at low temperature.[48] The H_2-TPR result is consistent with the styrene epoxidation experimental result.

Next, we performed density functional theory (DFT) calculations to gain an understanding of how the FeO_x nanocluster dictates the product selectivity. Figure 5 shows the calculated energy diagrams for the styrene oxidation pathways to styrene oxide and benzaldehyde (with the initial state set as 0.00). The red route represents the formation of styrene oxide: this reaction pathway starts from the peroxidic species ($HOO^{\bullet-}$) first adsorbing onto the FeO_x cluster supported on the Al_2O_3 (001) facet. Then cleavage of the O−OH bond occurs, which needs to overcome an energy barrier of 1.18 eV via a transition state (TS1SO),[49] followed by reacting with styrene via a Fe active center, yielding styrene oxide. Meanwhile, the reaction pathway to form benzaldehyde (the green route) indicates the decomposition of styrene to benzaldehyde and formic acid by interacting with superoxide species ($O_2^{\bullet-}$). The kinetics features of the green route revealed energy barriers of 0.39, 2.15, and 1.58 eV via transition states: formation of superoxide species (TS1BE), attack of superoxide species to styrene (TS2BE), and desorption of benzaldehyde from the catalyst (TS3BE). Apparently, styrene oxide is the more favorable product than benzaldehyde in the presence of Al_2O_3−FeO_x catalyst because the formation of styrene oxide has smaller energy barriers to overcome compared to that of benzaldehyde. The difference in free energy profiles for the two styrene oxidation pathways was confirmed by a temperature-dependence study. Figure S12a shows that when the reaction temperature increased to 85 °C, even though the conversion reached 93%, the selectivity toward styrene oxide decreased to 75% because a high reaction temperature helps overcome the energy barrier in the production of benzaldehyde. When the reaction temperature was decreased to 55 °C, the formation of benzaldehyde was further suppressed and the selectivity toward styrene oxide increased to 84%. A small quantity of styrene diol was also detected in this experiment, possibly because the oxidation of

https://doi.org/10.1021/acscatal.1c01366
ACS Catal. 2021, 11, 11542−11550

styrene to styrene diol in the absence of catalyst is thermodynamically spontaneous (Figure S12b; potential energies of reactants, intermediates; and final products are shown in Figure S13). Furthermore, the catalytic data of 6%-Al_2O_3−FeO_x at various temperatures (from 55 to 85 °C) were fitted in a pseudo-first-order model to study the kinetics. An Arrhenius plot of $-\ln k$ against $1/T$ was then plotted (Figure S14) to obtain the activation energy. By substituting the value of the slope in Figure S14, the activation energy of the reaction was determined to be 61.34 kJ/mol. This value is comparable to the previously reported value that was from catalytic systems that used acetonitrile, the same solvent as our catalytic experiment.[50−53]

Finally, we compared our Al_2O_3−FeO_x nanosheet catalyst with the state-of-the-art catalysts for styrene epoxidation in the literature. We categorized the existing catalysts into two groups based on the size of the active component in the catalyst. The first group is nano- or microsized catalysts. These catalysts used 3d transition metals (Co, Ni, Fe, Cu), group 4 and 5 metals (Ti, Si, Nb, V), or noble metals (Au and Ag) as the active components and graphene and carbon nanotube as the solid support.[25,54−67] As shown in Figure 6, some noble metal

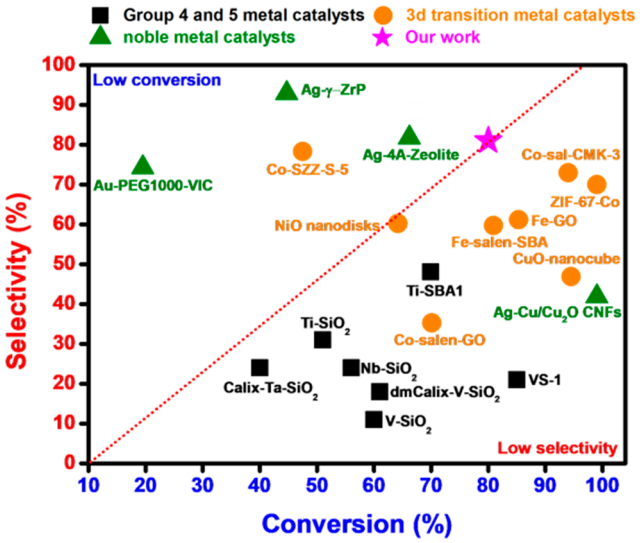

Figure 6. Comparison between the Al_2O_3−FeO_x nanosheet catalyst in this work (purple star) and the state-of-the-art catalysts for selective styrene oxidation to styrene oxide in terms of conversion and product selectivity.

catalysts such as Ag-γ-ZrP exhibited better selectivity for styrene oxide than our catalyst but suffered from low styrene conversion,[63] whereas 3d transition metal catalysts such as ZIF-67-Co achieved a higher styrene conversion than our catalyst but are limited by the low selectivity.[25] In comparison, our Al_2O_3−FeO_x nanosheet catalyst achieved the best combination of selectivity and conversion, both higher than 80%. The turnover frequency value (TOF) of those metal catalysts is shown in Table S2. The second group of catalysts is the recently reported nanocluster or single-atom catalysts. For example, Xiong et al. reported a pyrolyzing coordinated polymer strategy to obtain a single atomic site (SAS) Fe catalyst with a high yield of 64% and an excellent selectivity of 89% toward styrene oxide.[68] Compared with this SAS−Fe, our catalyst exhibits a comparable styrene oxide yield (64% at 70 °C and 70% at 85 °C). Another example is ligand-free Au nanoclusters confined in mesoporous silica,[69] which also produced a high styrene oxide yield of 64%. However, this Au nanocluster catalyst used an organic oxidant, *tert*-butyl hydroperoxide, which is less environmentally friendly than our catalyst that uses H_2O_2 as the oxidant. In addition, our nanosheet catalyst achieved a turnover frequency value of >280 h^{-1} that rivals the recently reported isolated single-atom Ru catalyst supported on the Lewis acid site of Beta zeolite.[70] Meanwhile, a TOF value comparison of our Al_2O_3−FeO_x catalysts with different Fe loading in Table S3 suggested that 4%-Al_2O_3−FeO_x exhibited the highest TOF value (476 h^{-1}) at 70 °C among those catalysts. Even though 6%-Al_2O_3−FeO_x contributed the best performance in terms of conversion and selectivity toward styrene oxide, the loss of its atomic efficiency is unavoidable as the size of the FeO_x clusters increase, giving a TOF value of 280 h^{-1}. When further increasing Fe loading, those Fe species would aggregate to nanoparticles (8%-Al_2O_3−FeO_x), resulting in a decrease of the TOF value (214 h^{-1}), as shown in Table S3.

CONCLUSION

In summary, we reported a simple wet-chemical route to prepare unsaturated FeO_x subnanoclusters supported on ultrathin amorphous Al_2O_3 nanosheets. As a catalyst for styrene epoxidation, this new material has achieved the combination of high selectivity and high conversion, selectively generating styrene oxide while suppressing the formation of overoxidized products such as 2-phenylacetaldehyde. The high catalytic performance originates from the stabilization of peroxidic species ($HOO^{\bullet-}$) by the Fe active sites of undercoordinated FeO_x subnanoclusters, promoting the styrene epoxidation pathway. The amorphous Al_2O_3 nanosheet stabilizes the catalytic FeO_x clusters and prevents them from sintering at high temperatures owing to its defective structure. The high thermal stability of the Al_2O_3−FeO_x nanosheet catalyst enables the regeneration of catalytic activity by heat treatment to effectively remove the organic adsorbates that block the catalytic sites without destructing the catalyst structure. Our work showcases the importance of choosing the right combination of nanocluster catalyst, support, and catalyst−support interaction in achieving the desired catalytic performance.

ASSOCIATED CONTENT

Supporting Information

The Supporting Information is available free of charge at https://pubs.acs.org/doi/10.1021/acscatal.1c01366.

Comparison between product yields with or without the addition of isopropyl using 6%-Al_2O_3−FeO_x as the catalyst; SEM images, XRD patterns, and HAADF-STEM images of 6%-Al_2O_3−FeO_x and C-6%-Al_2O_3−FeO_x; comparison of Fe 2p XPS spectra before and after running catalytic test 4 times; EXAFS spectra fitting results; product yield using 6%-Al_2O_3−FeO_x as catalyst under different reaction conditions; catalytic properties of various Al_2O_3−FeO_x samples for styrene epoxidation with H_2O_2 as the oxidant; EXAFS fitting parameters at the Fe K-edge for various samples (S_0^2 = 0.79) (PDF)

https://doi.org/10.1021/acscatal.1c01366
ACS Catal. 2021, 11, 11542−11550

AUTHOR INFORMATION

Corresponding Authors

Lin Guo − *School of Chemistry, Beijing Advanced Innovation Center for Biomedical Engineering, Key Laboratory of Bio-Inspired Smart Interfacial Science and Technology, Beihang University, Beijing 100191, China;* orcid.org/0000-0002-6070-2384; Email: guolin@buaa.edu.cn

Long Luo − *Department of Chemistry, Wayne State University, Detroit, Michigan 48202, United States;* orcid.org/0000-0001-5771-6892; Email: long.luo@wayne.edu

Authors

Zhao Yang − *School of Chemistry, Beijing Advanced Innovation Center for Biomedical Engineering, Key Laboratory of Bio-Inspired Smart Interfacial Science and Technology, Beihang University, Beijing 100191, China*

Shuo Zhang − *Shanghai Synchrotron Radiation Facility, Shanghai Institute of Applied Physics, Chinese Academy of Science, Shanghai 201204, China;* orcid.org/0000-0002-3715-8632

Hewei Zhao − *School of Chemistry, Beijing Advanced Innovation Center for Biomedical Engineering, Key Laboratory of Bio-Inspired Smart Interfacial Science and Technology, Beihang University, Beijing 100191, China*

Anran Li − *Beijing Advanced Innovation Center for Big Data-Based Precision Medicine, School of Medicine and Engineering, Beihang University, Beijing 100191, China;* orcid.org/0000-0003-1399-8407

Complete contact information is available at: https://pubs.acs.org/10.1021/acscatal.1c01366

Author Contributions

[§]Z.Y. and S.Z.: These authors contributed equally to this work.

Author Contributions

Z.Y., H.Z., and L.G. designed and directed the study. Z.Y. conceived and performed the fabrication work. S.Z. performed XAFS and analyzed the results. A.L. performed the first-principles calculations and analyzed the results. Z.Y. performed the spherical aberration-corrected transmission electron microscopy. L.L., H.Z., and L.G. participated with characterization and data analysis. All authors contributed to the discussion. Z.Y., L.L., and L.G. wrote the manuscript. All authors reviewed the paper.

Notes

The authors declare no competing financial interest.

ACKNOWLEDGMENTS

The work performed at Beihang University was supported by the National Natural Science Foundation of China (51532001, 51802010, and 52073008) and the Academic Excellent Foundation of BUAA for PhD Students.

REFERENCES

(1) Valden, M.; Lai, X.; Goodman, D. W. Onset of catalytic activity of gold clusters on titaniawith the appearance of nonmetallic properties. *Science.* **1998**, *281*, 1647−1650.

(2) Turner, M.; Golovko, V. B.; Vaughan, O. P. H.; Abdulkin, P.; Berenguer-Murcia, A.; Tikhov, M. S.; Johnson, B. F. G.; Lambert, R. M. Selective oxidation with dioxygen by gold nanoparticle catalysts derived from 55-atom clusters. *Nature* **2008**, *454*, 981−983.

(3) Yamazoe, S.; Koyasu, K.; Tsukuda, T. Nonscalable oxidation catalysis of gold clusters. *Acc. Chem. Res.* **2014**, *47*, 816−824.

(4) Kwak, K.; Choi, W.; Tang, Q.; Kim, M.; Lee, Y.; Jiang, D.; Lee, D. A molecule-like $PtAu_{24}(SC_6H_{13})_{18}$ nanocluster as an electrocatalyst for hydrogen production. *Nat. Commun.* **2017**, *8*, 14723−14730.

(5) Hakkinen, H. The gold-sulfur interface at the nanoscale. *Nat. Chem.* **2012**, *4*, 443−455.

(6) Liu, J.; Jiao, M.; Mei, B.; Tong, Y.; Li, Y.; Ruan, M.; Song, P.; Sun, G.; Jiang, L.; Wang, Y.; Jiang, Z.; Gu, L.; Zhou, Z.; Xu, W. Carbon-supported divacancy-anchored platinum single-atom electrocatalysts with superhigh Pt utilization for the oxygen reduction reaction. *Angew. Chem., Int. Ed.* **2019**, *58*, 1163−1167.

(7) Yang, S.; Tak, Y. J.; Kim, J.; Soon, A.; Lee, H. Support effect in single-atom platinum catalysts for electrochemical oxygen reduction. *ACS Catal.* **2017**, *7*, 1301−1307.

(8) Cheng, N.; Stambula, S.; Wang, D.; Banis, M. N.; Liu, J.; Riese, A.; Xiao, B.; Li, R.; Sham, T. K.; Liu, L. M.; Botton, G. A.; Sun, X. Platinum single-atom and cluster catalysis of the hydrogen evolution reaction. *Nat. Commun.* **2016**, *7*, 13638.

(9) Wei, H.; Liu, X.; Wang, A.; Zhang, L.; Qiao, B.; Yang, X.; Huang, Y.; Miao, S.; Liu, J.; Zhang, T. FeO_x-supported platinum single-atom and pseudo-single-atom catalysts for chemoselective hydrogenation of functionalized nitroarenes. *Nat. Commun.* **2014**, *5*, 5634.

(10) Schrader, I.; Warneke, J.; Backenkohler, J.; Kunz, S. Functionalization of platinum nanoparticles with L-proline: simultaneous enhancements of catalytic activity and selectivity. *J. Am. Chem. Soc.* **2015**, *137*, 905−912.

(11) Zhang, B.; Asakura, H.; Zhang, J.; Zhang, J.; De, S.; Yan, N. Stablilizing a platinum single-atom catalyst on supported phosphomolybdic acid without compromising hydrogenation activity. *Angew. Chem., Int. Ed.* **2016**, *55*, 8319−8323.

(12) Hall, M. D.; Foran, G. J.; Zhang, M.; Beale, P. J.; Hambley, T. W. XANES determination of the platinum oxidation state distribution in cancer cells with platinum (IV) anticancer agents. *J. Am. Chem. Soc.* **2003**, *125*, 7524−7525.

(13) Zhang, Z.; Zhu, Y.; Asakura, H.; Zhang, B.; Zhang, J.; Zhou, M.; Han, Y.; Tanaka, T.; Wang, A.; Zhang, T.; Yan, N. Thermally stable single atom $Pt/m\text{-}Al_2O_3$ for selective hydrogenation and CO oxidation. *Nat. Commun.* **2017**, *8*, 16100.

(14) Wu, Z.; Dang, D.; Tian, X. Designing robust support for Pt alloy nanoframes with durable oxygen reduction reaction activity. *ACS Appl. Mater. Interfaces* **2019**, *11*, 9117−9124.

(15) Shao, Q.; Li, F.; Chen, Y.; Huang, X. The advanced designs of high-performance platinum-based electrocatalysis: recent progress and challenges. *Adv. Mater. Interfaces* **2018**, *5*, 1800486.

(16) Stephens, I.; Rossmeisl, J.; Chorkendorff, I. Toward sustainable fuel cells. *Science* **2016**, *354*, 1378−1379.

(17) Wang, Z.; Sun, K.; Henzie, J.; Hao, X.; Li, C.; Takei, T.; Kang, Y. M.; Yamauchi, Y. Spatially confined assembly of monodisperse ruthenium nanoclusters in a hierarchically ordered carbon electrode for efficient hydrogen evolution. *Angew. Chem., Int. Ed.* **2018**, *57*, 5848−5852.

(18) Liu, L.; Zhao, X.; Li, R.; Su, H.; Zhang, H.; Liu, Q. Subnano amorphous Fe-based clusters with high mass activity for efficient electrocatalytic oxygen reduction reaction. *ACS Appl. Mater. Interfaces* **2019**, *11*, 41432−41439.

(19) Jun, S.; Joo, S. H.; Ryoo, R.; Kruk, M.; Jaroniec, M.; Liu, Z.; Ohsuna, T.; Terasaki, O. Synthesis of new, nanoporous carbon with hexagonally ordered mesostructure. *J. Am. Chem. Soc.* **2000**, *122*, 10712−10713.

(20) Patil, M. V.; Yadav, M. K.; Jasra, R. V. Catalytic epoxidation of α-pinene with molecular oxygen using cobalt(II)-exchanged zeolite Y-based heterogeneous catalysts. *J. Mol. Catal. A: Chem.* **2007**, *277*, 72−80.

(21) Wang, X.; Wu, S.; Li, Z.; Yang, X.; Su, H.; Hu, J.; Huo, Q.; Guan, J.; Kan, Q. Cu(II), Co(II), Fe(III) or VO(II) schiff base complexes immobilized onto CMK-3 for styrene epoxidation. Microporous and mesoporous materials. *Microporous Mesoporous Mater.* **2016**, *221*, 58−66.

(22) Zhu, C.; Shi, Q.; Xu, B. Z.; Fu, S.; Wan, G.; Yang, C.; Yao, S.; Song, J.; Zhou, H.; Du, D.; Beckman, S. P.; Su, D.; Lin, Y.

Hierarchically porous M-N-C (M = Co and Fe) single-atom electrocatalysts with robust MNx active moieties enable enhanced ORR performance. *Adv. Energy Mater.* **2018**, *8*, 1801956.
(23) Tian, S.; Fu, Q.; Chen, W.; Feng, Q.; Chen, Z.; Zhang, J.; Cheong, W. C.; Yu, R.; Gu, L.; Dong, J.; Luo, J.; Chen, C.; Peng, Q.; Draxl, C.; Wang, D.; Li, Y. Carbon nitride supported Fe2 cluster catalysts with superior performance for alkene epoxidation. *Nat. Commun.* **2018**, *9*, 2353.
(24) Yang, Y.; Guan, J.; Qiu, P.; Kan, Q. Enhanced catalytic performances by surface silylation of Cu(II) schiff base-containing SBA-15 in epoxidation of styrene with H_2O_2. *Appl. Surf. Sci.* **2010**, *256*, 3346−3351.
(25) Hui, J.; Chu, H.; Zhang, W.; Shen, Y.; Chen, W.; Hu, Y.; Liu, W.; Gao, C.; Guo, S.; Xiao, G.; Li, S.; Fu, Y.; Fan, D.; Zhang, W.; Huo, F. Multicomponent metal-organic framework derivatives for optimizing the selectivity catalytic performance of styrene epoxidation reaction. *Nanoscale* **2018**, *10*, 8772−8778.
(26) Wang, Q.; Liang, X.; Bi, R.; Liu, Y.; He, Y.; Feng, J.; Li, D. Highly efficient CuCr-MMO catalyst for a base-free styrene epoxidation with H_2O_2 as the oxidant: synergistic effect between Cu and Cr. *Daltron Trans.* **2019**, *48*, 16402−16411.
(27) Zhao, H.; Zhu, Y.; Li, F.; Hao, R.; Wang, S.; Guo, L. A generalized strategy for synthesis of large-size ultrathin two-dimensional metal oxide nanosheets. *Angew. Chem., Int. Ed.* **2017**, *56*, 8766−8770.
(28) Zhou, X.; Yin, Y. X.; Wan, L. J.; Guo, Y. G. Self-assembled nanocomposite of silicon nanoparticles encapsulated in graphene through electrostatic attraction for lithium-ion batteries. *Adv. Energy. Mater.* **2012**, *2*, 1086−1090.
(29) Boyd, G. E.; Adamson, A. W.; Myers, L. S. The exchange adsorption of ions from aqueous solutions by organic zeolites. III. kinetics. *J. Am. Chem. Soc.* **1947**, *69*, 2836−2848.
(30) Allen, M. J.; Tung, V. C.; Kaner, R. B. Honeycomb carbon: A review of graphene. *Chem. Rev.* **2010**, *110*, 132−145.
(31) Thornburg, N. E.; Thompson, A. B.; Notestein, J. M. Periodic trends in highly dispersed group IV and V supported metal oxide catalysts for alkene epoxidation with H_2O_2. *ACS Catal.* **2015**, *5*, 5077−5088.
(32) Bregante, D. T.; Thornburg, N. E.; Notestein, J. M.; Flaherty, D. W. Consequences of confinement for alkene epoxidation with hydrogen peroxide on highly dispersed group 4 and 5 metal oxide catalysts. *ACS Catal.* **2018**, *8*, 2995−3010.
(33) Feng, Q.; Song, Q. Aldehydes and ketones formation: Copper-catalyzed aerobic oxidative decarboxylation of phenylacetic acids and α-hydroxyphenlacetic acids. *J. Org. Chem.* **2014**, *79*, 1867−1871.
(34) Ignacio-De Leon, P. A. A.; Contreras, C. A.; Thornburg, N. E.; Thompson, A. B.; Notestein, J. M. Catalyst structure and substituent effects on epoxidaiton of styrenics with immobilized Mn(tmtacn) complexes. *Appl. Catal., A* **2016**, *511*, 78−86.
(35) Hansen, T. W.; Delariva, A. T.; Challa, S. R.; Datye, A. K. Sintering of catalytic nanoparticles: Particle migration or Ostwald ripening. *Acc. Chem. Res.* **2013**, *46*, 1720−1730.
(36) Fukamori, Y.; Konig, M.; Yoon, B.; Wang, B.; Esch, F.; Heiz, U.; Landman, U. Fundamental insight into the substrate-dependent ripening of monodisperse clusters. *ChemCatChem* **2013**, *5*, 3330−3341.
(37) Wettergren, K.; Schweinberger, F. F.; Deiana, D.; Ridge, C. J.; Crampton, A. S.; Rotzer, M. D.; Hansen, T. W.; Zhdanov, V. P.; Heiz, U.; Langhammer, C. High sintering resistance of size-selected platinum cluster catalysts by suppressed Ostwald ripening. *Nano Lett.* **2014**, *14*, 5803−5809.
(38) Ouyang, R.; Liu, J. X.; Li, W. X. Atomistic theory of Ostwald ripening and disintegration of supported metal particles under reaction conditions. *J. Am. Chem. Soc.* **2013**, *135*, 1760−1771.
(39) Watanabe, R.; Saito, Y.; Fukuhara, C. Dehydrogenation of ethylbenzene over zirconium-based perovskite-type catalysts of $AZrO_3$ (A: Ca, Sr, Ba). *Appl. Catal., A* **2014**, *482*, 344−351.
(40) Zhao, C.; Huang, B.; Xie, E.; Zhou, J.; Zhang, Z. Improving gas-sensing properties of electrospun In_2O_3 nanotubes by Mg acceptor doping. *Sens. Actuators, B* **2015**, *207*, 313−320.
(41) Li, H.; Du, K.; Xiang, C.; An, P.; Shu, X.; Dang, Y.; Wu, C.; Wang, J.; Du, W.; Zhang, J.; Li, S.; Tian, H.; Wang, S.; Xia, H. Controllable chelation between tannic acid and Fe precursors to obtain N, S co-doped carbon with high density Fe-single atom-nanoclusters for highly efficient oxygen reduction reaction in Zn-air batteries. *J. Mater. Chem. A* **2020**, *8*, 17136−17149.
(42) Cai, Z.; Zhou, D.; Wang, M.; Bak, S. M.; Wu, Y.; Wu, Z.; Tian, Y.; Xiong, X.; Li, Y.; Liu, W.; Siahrostami, S.; Kuang, Y.; Yang, X. Q.; Duan, H.; Feng, Z.; Wang, H.; Sun, X. Introducing Fe^{2+} into nickel-iron layered double hydroxide: Local structure modulated water oxidation activity. *Angew. Chem., Int. Ed.* **2018**, *57*, 9392−9396.
(43) Yu, H. Y.; Li, M. F.; Cho, B. J.; Yeo, C. C.; Joo, M. S.; Kwong, D.-L.; Pan, J. S.; Ang, C. H.; Zheng, J. Z.; Ramanathan, S. Energy gap and band alignment for $(HfO_2)_x(Al_2O_3)_{1-x}$ on (100) Si. *Appl. Phys. Lett.* **2002**, *81*, 376−378.
(44) Wang, H.; Zhang, J.; Hang, X.; Zhang, X.; Xie, J.; Pan, B.; Xie, Y. Half-metallicity in single-layered manganese dioxide nanosheets by defect engineering. *Angew. Chem., Int. Ed.* **2015**, *54*, 1195−1199.
(45) Lin, Z.; Yin, A.; Mao, J.; Xia, Y.; Kempf, N.; He, Q.; Wang, Y.; Chen, C. Y.; Zhang, Y.; Ozolins, V.; Ren, Z.; Huang, Y.; Duan, X. Scalable solution-phase epitaxial growth of symmetry-mismatched heterostructures on two-dimensional crystal soft template. *Sci. Adv.* **2016**, *2*, e1600993−9.
(46) Frenkel, A. I.; Ehre, D.; Lyahovitskaya, V.; Kanner, L.; Wachtel, E.; Lubomirsky, I. Orgin of polartiy in amorphous $SrTiO_3$. *Phys. Rev. Lett.* **2007**, *99*, 215502.
(47) Sierra-Pereira, C.; Urquieta-Gonzalez, E. Reduction of NO with CO on CuO or Fe_2O_3 catalysts supported on TiO_2 in the presence of O_2, SO_2 and water steam. *Fuel* **2014**, *118*, 137−147.
(48) Wang, D.; Hao, Z.; Cheng, D.; Shi, X. Influence of the calcination temperature on the $Au/FeO_x/Al_2O_3$ catalyst. *J. Chem. Technol. Biotechnol.* **2006**, *81*, 1246−1251.
(49) Fu, H.; Huang, K.; Yang, G.; Cao, Y.; Wang, H.; Peng, F.; Wang, Q.; Yu, H. Synergistic effect of nitrogen dopants on carbon nanotubes on the catalytic selective epoxidation of styrene. *ACS Catal.* **2020**, *10*, 129−137.
(50) Tan, K. H.; Iqbal, A.; Adam, F.; Abu Bakar, N. H. H.; Ahmad, M. N.; Yusop, R. M.; Pauzi, H. Influence of Mg/CTAB ratio on the structural, physicochemical properties and catalytic activity of amorphous mesoporous magnesium silicate catalysts. *RSC Adv.* **2019**, *9*, 38760−38771.
(51) Guo, S.; Liang, Y.; Tricard, S.; Wang, N.; Feng, L.; He, S.; Zheng, P.; Zhao, J.; Fang, J. Effect of cesium ion on the synthesis and catalytic properties with FeCo Prussian blue analogue. *Chem. Phys. Lett.* **2018**, *710*, 180−187.
(52) Liu, J.; Meng, R.; Li, J.; Jian, P.; Wang, L.; Jian, R. Achieving high-performance for catalytic epoxidation of styrene with uniform magnetically separable $CoFe_2O_4$ nanoparticles. *Appl. Catal., B* **2019**, *254*, 214−222.
(53) Yuan, X.; Wang, Q.; Horner, J. H.; Sheng, X.; Newcomb, M. Kinetics and activation parameters for oxidations of styrene by compounds I from the cytochrome P450 (BM-3) (CYP102A1) heme domain and from CYP119. *Biochemistry* **2009**, *48*, 9140−9146.
(54) Hu, C.; Zhang, L.; Zhang, J.; Cheng, L.; Zhai, Z.; Chen, J.; Hou, W. Template-free method to prepare porous Cu-containing nanotubes with a good catalytic performance for styrene epoxidation. *Appl. Surf. Sci.* **2014**, *298*, 116−124.
(55) Hu, L.; Yue, B.; Wang, C.; Chen, X.; He, H. Enhanced catalytic activity over vanadium-containing silylated SBA-15 catalysts for styrene epoxidation and benzene hydroxylation. *Appl. Catal., A* **2014**, *477*, 141−146.
(56) Tanglumlert, W.; Imae, T.; White, T. J.; Wongkasemjit, S. Styrene oxidation with H_2O_2 over Fe- and Ti-SBA-1 mesoporous silica. *Catal. Commun.* **2009**, *10*, 1070−1073.

https://doi.org/10.1021/acscatal.1c01366
ACS Catal. 2021, 11, 11542−11550

(57) Hu, X.; Bai, J.; Li, C.; Liang, H.; Sun, W. Silver-based 4A zeolite composite catalyst for styrene epoxidaiton by one-pot hydrothermal synthesis. *Eur. J. Inorg. Chem.* **2015**, *2015*, 3758−3763.
(58) Singh, B.; Sinha, A. K. Synthesis of hierarchical mesoporous vanadium silicate-1 zeolite catalyst for styrene epoxidation with organic hydroperoxide. *J. Mater. Chem. A* **2014**, *2*, 1930−1939.
(59) Zeng, A.; Li, Y.; Su, S.; Li, D.; Hou, B.; Yu, N. Gold nanoparticles stabilized by task-specific ionic complexes: Quasi-homogeneous catalysts with self-separating nature for aerobic epoxidation of styrene. *J. Catal.* **2014**, *319*, 163−173.
(60) Su, H. L.; Wu, S.; Li, Z.; Huo, Q.; Guan, J.; Kan, Q. Co(II), Fe(III), or VO(II) Schiff base metal complexes immobilized on graphene oxide for styrene epoxidation. *Appl. Organomet. Chem.* **2015**, *29*, 462−467.
(61) Jinka, K. M.; Pai, S. M.; Newalkar, B. L.; Choudary, N. V.; Jasra, R. V. Co-SSZ-51 as a catalyst for styrene epoxidation using molecular oxygen. *Catal. Commun.* **2010**, *11*, 638−642.
(62) Li, Z.; Wu, S.; Ding, H.; Zheng, D.; Hu, J.; Wang, X.; Huo, Q.; Guan, J.; Kan, Q. Immobilized Cu(II) and Co (II) salen complexes on grapheme oxide and their catalytic activity for aerobic epoxidation of styrene. *New J. Chem.* **2013**, *37*, 1561−1568.
(63) Sun, J.; Yu, G.; Huo, Q.; Kan, Q.; Guan, J. Epoxidation of styrene over Fe (Cr)-ML-101 metal-organic frameworks. *RSC Adv.* **2014**, *4*, 38048−38054.
(64) Ren, S.; Yang, C.; Sun, C.; Hui, Y.; Dong, Z.; Wang, J.; Su, X. Novel NiO nanodisks and hollow nanodisks derived from $Ni(OH)_2$ nanostructures and their catalytic performance in epoxidation of styrene. *Mater. Lett.* **2012**, *80*, 23−25.
(65) Hu, X.; Bai, J.; Hong, H.; Li, C. Synthesis of Ag-loaded 4A-zeolite composite catalyst via supercritical CO_2 fluid for styrene epoxidation. *Microporous Mesoporous Mater.* **2016**, *228*, 224−230.
(66) Wang, Q.; Li, C.; Bai, J.; Sun, W.; Wang, J. A simple method to prepare bimetallic Ag-Cu/Cu_2O carbon fibers applied in the regulation of styrene epoxidation reaction. *J. Inorg. Organomet. Polym. Mater.* **2016**, *26*, 488−493.
(67) Liu, J.; Wang, F.; Gu, Z.; Xu, X. Styrene epoxidation over Ag-γ-ZrP catalyst prepared by ion-exchange. *Catal. Commun.* **2009**, *10*, 868−871.
(68) Xiong, Y.; Sun, W.; Xin, P.; Chen, W.; Zheng, X.; Yan, W.; Zheng, L.; Dong, L.; Zhang, L.; Wang, D.; Li, Y. Gram-scale synthesis of high-loading single-atomic-site Fe catalysts for effective epoxidation of styrene. *Adv. Mater.* **2020**, *32*, 2000896.
(69) Al-Shankiti, B.; Al-Maksoud, W.; Habeeb Muhammed, M. A.; Anjum, D. H.; Moosa, B.; Basset, J.-M.; Khashab, N. M. Ligand-free gold nanoclusters confined in mesoporous silica nanoparticles for styrene epoxidation. *Nanoscale Adv.* **2020**, *2*, 1437−1442.
(70) Yang, H.; Liu, Q.; Li, Y.; Sun, K.; Chen, Z.; Peng, Q.; Chen, C. Isolated single-atom ruthenium anchored on beta zeolite as an efficient heterogeneous catalyst for styrene epoxidation. *ChemNanoMater.* **2020**, *6*, 1647−1651.

https://doi.org/10.1021/acscatal.1c01366
ACS Catal. 2021, 11, 11542−11550